LBL-21640



# VITRIFICATION OF Y ZEOLITE AND ITS EFFECTS ON HREM IMAGES

R. Csencsits
(M.S. Thesis)

April 1986



Lawrence Berkeley Laboratory
University of California
Berkeley, California 94720

Prepared for the U.S. Department of Energy
under Contract DE-AC03-76SF00098

Center for Advanced Materials

## DISCLAIMER



# VITRIFICATION OF Y ZEOLITE AND ITS EFFECTS ON HREM IMAGES

Roseann Csencsits

Center for Advanced Materials
University of California
and
Materials Science & Mineral Engineering
University of California
Berkeley, CA 94720 USA

May 1986

Master's Thesis

# TABLE OF CONTENTS


ACKNOWLEDGEMENTS ..... ii

ABSTRACT ..... iii

1. INTRODUCTION ..... 1

2. DAMAGE IN THE TEM ..... 6

2.1. Theory ..... 6

2.1.1 Knock-on damage ..... 6

2.1.2 Radiolytic damage ..... 8

2.2. Experimental Procedure ..... 10

2.3. Results ..... 11

2.4. Conclusions ..... 13

3. COMPUTER IMAGE SIMULATION ..... 15

3.1. Introduction ..... 15

3.2. Computations ..... 16

3.3. Results ..... 17

3.4. Conclusions ..... 19

APPENDIX: CONSTRUCTION OF COMPUTATIONAL CELL ..... 21

REFERENCES ..... 26

FIGURE CAPTIONS ..... 28

FIGURES ..... 30

# ACKNOWLEDGEMENTS

There are many people who have helped me reach this point and I would like to thank them.

Professor Ronald Gronsky, my advisor, who supported this project and remained enthusiastic throughout the past three years. Professors Gabor Somorjai and Andreas Glaeser for reviewing this thesis.

Dave Ackland for always providing the necessary technical assistance and for keeping the microscopes in top working order. Caroline Schooley for microtomy instructions and for making available "state of the art" specimen preparation facilities.

Mike O'Keefe and Roar Kilaas for trying to teach me something about phase contrast imaging and image simulation.

Ignatious Chan for many fruitful discussions.

Jamie Rose for pointing out the obvious when it is so easily overlooked.

The Gronsky group for sharing and adding to the experience.

Mike for your linear thinking, some day you will meet your match!

Charlene, Eileen, Eduardo, Roar, Jamie and Mike thanks for all the fun.

Max for your independence and inter-dependence.

This work has been funded by the Director, Office of Energy Research, Office of Basic Energy Sciences, Materials Science Division of the U. S. Department of Energy under Contract No. DE-AC03-76SF00098.

# ABSTRACT

Electron diffraction has been used to study the vitrification of Y zeolite in the transmission electron microscope (TEM). Calculations and experimental evidence have confirmed that in the range 80-200kV, the damage of Y zeolites is radiolytic in the TEM. Incident beam electrons interact with specimen electrons which leads to a rearrangement of the structure. The proposed mechanism for this transformation involves enhancement of structural relaxation at Al sites due to the presence of a charge compensating cation.

Computer image simulation was used to assess the effects of damage on high resolution electron microscope (HREM) images of Y zeolites. Simulated images of perfect Y zeolite revealed that only for a specimen 10-20nm thick would the HREM image be a structure image at Scherzer defocus (-60nm); at thickness greater than 20nm the images contain non-structural detail due to second order interferences. At larger defocus values (-100nm), thicker crystals (60nm) "with 30-50% of their thickness amorphous" produce images which can be related to the structure because the presence of the amorphous material decreases the visibility of the non-structural detail.

# 1. INTRODUCTION

Zeolites are crystalline alumino-silicates that have been known for over 200 years. Originally they were used for ion exchange procedures and extensively as water absorbents. In modern times zeolites have found widespread application as industrial catalysts and catalyst supports. The zeolites act as part of heterogeneous catalyst systems and their catalytic activity is often related to their crystallographic structures.

On the atomic level all zeolites are made up of a framework in which silicon and aluminum atoms are surrounded tetrahedrally by oxygen atoms that link to other tetrahedrally bonded silicon and aluminum atoms. This generates a porous structure with cages and channels of various shapes and sizes depending on the topology of the particular zeolite. Stoichiometrically a zeolite may be represented (Thomas et al., 1982) as

$$M_{n/x} \cdot nAlO_2 \cdot mSiO_2 \cdot wH_2O$$

where x is the valence of the cation M, n is the number of Al substitutions per (n+m) Si atom sites in the unit cell and w is the number of water molecules occluded in the structure.

Zeolite Y is topologically similar to faujasite (fig. 1) (Smith, 1976) with a cubic unit cell (Breck, 1974; Meier and Olsen, 1971). The cell dimension is almost 2.5nm, containing 192 $(Si,Al)O_4$ tetrahedra. The structure is stable and rigid while containing a void space of about 50 vol% of the dehydrated crystal. Zeolite Y and faujasite differ in cation composition and distribution, the Si/Al-ratio and possible Si-Al ordering in tetrahedral sites.

The typical unit cell formulae of zeolite Y and faujasite are

$$Na_{56}\,[(AlO_2)_{56}\,(SiO_2)_{136}]\cdot 250H_2O$$

$$Na_{12}\,Ca_{12}\,Mg_{11}\,[(AlO_2)_{59}\,(SiO_2)_{133}]\cdot 235H_2O$$

respectively. The faujasite-type alumino-silicate framework consists of a face centered cubic lattice with a building block of two connected sodalite cages. A sodalite cage is a cubo-octahedron made up of 24 tetrahedral metal atoms connected through oxygen atoms to form six 6-member rings and six 4-member rings (counting only metal atoms) (fig.2). The sodalite cages are linked tetrahedrally via the 6-member rings. The faujasite-type zeolites have a three dimensional channel system, parallel to the <110> directions, with approximately 0.74nm and 0.22nm diameter apertures. Figure 3 shows the nature of the internal surface of the zeolite. The cations can occupy three positions in zeolite Y; they may be within the hexagonal prisms joining the sodalite cages, adjacent to the six member rings or within the main channels. Infrared spectra, adsorption data and conductivity measurements suggest that the cations and water molecules behave as a strong electrolyte solution and float freely throughout the framework.

Zeolite Y is crystallized (Lechert, 1984) at or below 100°C, from a sodium alumino-silicate gel/solution mixture, that uses a colloidal silica sol as the silica source. The composition of the reaction mixture is defined by a set of molar ratios

$$\frac{SiO_2}{Al_2O_3},\ \frac{H_2O}{SiO_2},\ \frac{OH^-}{SiO_2},\ \frac{M^+}{SiO_2}$$

where $M^+$ is usually the Na-ion, but may be other alkali-, alkaline earth- or ammonium ions. Some special zeolites have been prepared with the addition of quaternary ammonium salts, amines or other polar organic substances. The relatively large organic ions are regarded as templates around which the zeolite structure can be formed in the

reaction mixture, and in these cases the ratio $\frac{R_4N^+}{SiO_2}$ must be added to complete the definition of the batch composition.

The framework structure and composition of the zeolite is determined mainly by the composition and temperature of the gel. The nucleation and growth phenomena that control the zeolite crystallization process are very complex. Gel aging time, the pH of the mixture and the temperature are all important variables.

The Si/Al-ratio of a zeolite is an important parameter because it determines the structural stability of the zeolite at elevated temperatures. "Ultrastable" zeolites may be prepared by the replacement of the aluminum in the alumino-silicate lattice by silicon. This is commonly achieved by a hydrothermal treatment (steam treatment at elevated temperatures) of the ammonium form of the zeolite followed by acid leaching. De-aluminated Y zeolite, almost aluminum-free Y zeolite has been obtained (Klinowski et al, 1981) by passing dry nitrogen gas saturated with $SiCl_4$ over the zeolite at 400–470°C (Beyer and Belenykaja, 1980). The aluminum is released as $AlCl_3$, and the zeolite is thermally more stable.

For most hydrocarbon transformation reactions requiring acidity, the alkali metal ion-containing forms of the zeolites are relatively inactive. A zeolite commonly used for hydrocarbon transformations is a hydrogen ion-exchanged Y zeolite. Zeolite HY is produced by heating a $NH_4^+$-exchanged Y zeolite at 250–400°C in an inert atmosphere (Poutsma, 1976). The heating results in the stoichiometric evolution of $NH_3$ and loss of adsorbed water.

Since the late 1950's zeolites have been used in the processing of petroleum. Zeolites in the acid form have greater catalytic activity for cracking reactions than their

predecessors, amorphous alumino-silicates. The shape selectivity of the zeolites can be used in petroleum refining reactions: dewaxing, reforming and isomerization.

Cracking is an acid catalyzed reaction. The Brönsted acid sites in alumino-silicates are located at the four coordinated aluminum sites ($AlO_4^-$ with its associated $H^+$), so the number of acid sites is dependent on the Si/Al-ratio. As the Si/Al-ratio increases there is a loss of potential acid sites but no reduction in the acid strength of the remaining sites. The Brönsted acidity of amorphous alumino-silicates is the same as that of superacids (Fraissard, 1980) although the cause of the superacidity is unkown. Zeolite HY is often 3-4 orders of magnitude more active as a cracking catalyst than amorphous alumino-silicates (Miale et al, 1966), however its Brönsted acid strength is similar. The number of Brönsted sites is greater for HY due to its large internal surface area, but this is not able to explain the "superactivity" of HY. The activity of HY zeolite in cracking reactions is technologically exploited while it is not understood.

In addition to cracking, Y zeolites are used to convert methanol into olefins and aromatics. Since both the conversion of methanol to gasoline and the cracking of petroleum require elevated temperatures, the dealuminated Y zeolite is preferred. The increased stability prolongs its catalytic lifetime over that of non-stabilized Y zeolite, without a significant loss in activity.

Ideally, a catalyst is a substance that increases the rate of a reaction and can be recovered unchanged at the end of the reaction (Castellan, 1971), however, this is seldom realized. Usually a zeolite undergoes small changes each time it is used, and after prolonged usage it no longer functions as a catalyst. This process of destruction of the catalyst is still to be understood on the molecular level. The catalytic activity or selectivity of a zeolite may be related to its microstructure; ie., if the channels do not pass

completely through the crystal the reactive species will not be able to diffuse in or out. High resolution transmission electron microscopy provides real space structure information with very high spatial resolution. Zeolite microstructure studied using high resolution transmission electron microscopy (HREM) may provide insight into the zeolite activity or selectivity and the destruction of these properties. Defects such as intergrowths of ZSM-5 in ZSM-11 (Thomas and Millward, 1982) could result in different product selectivity because of different types of cavities formed at the channel intersections. Coking, the formation of various carbonaceous compounds on the internal and external surfaces of catalysts, can deactivate catalytic sites or make them inaccessible by pore blockage (Bibby, 1986). This structural information revealed by HREM could be combined with catalytic activity and selectivity studies to help better understand catalytic reaction mechanisms and the catalyst destruction processes.

The difficulty with doing a high resolution transmission electron microscopy study on zeolites is that they damage under electron irradiation (fig.4). The crystalline zeolites undergo a phase transformation known in the geological community as the metamict transformation; the zeolite becomes amorphous during irradiation. This loss of long-range order appears to be similar to observations of other crystalline systems with $SiO_4$ tetrahedra (Pabst, 1952); the damage rate of zeolites shows dependence on the amount of hydration (Bursill et al, 1980), on the size of the cations (Bursill et al, 1981) and on the Si/Al-ratio (Chan, 1984). This thesis is the first systematic investigation of the damage of Y zeolites in the transmission electron microscope; the goal of the study is to determine the mechanism for electron damage as well as its effects on high resolution images.

# 2. DAMAGE IN THE TEM

## 2.1 Theory

The types of damage possible in the transmission electron microscope (TEM) can be classified under two headings: knock-on and radiolytic. "Knock-on" damage involves the interaction of the incident electron with the core of an atom in the specimen. The atom is "knocked" from its site, leaving the structure changed. Radiolytic damage involves the transfer of energy from the incident electron to the electrons in the specimen. The increase in energy of the specimen electrons results in bond breakage and consequently the possible relaxation of the structure.

### 2.1.1 Knock-on damage

The cross-section for direct interaction of the probing electron and the nuclear core of an atom in the specimen is called the knock-on cross-section. For relativistic electrons this cross-section is given by (McKinley and Feshbach, 1948; Seitz and Koehler, 1956)

$$\sigma_n = \left\{ \frac{4\pi a_o^2 U_R^2}{(mc^2)^2} \right\} \left\{ \frac{Z^2(1-\beta^2)}{\beta^4} \right\} \left\{ \left(\Omega_r\right) + 2\pi\alpha\beta \left(\Omega_r\right)^{1/2} - (\beta^2+\pi\alpha\beta) \ln\left(\Omega_r\right) - 1 - 2\pi\alpha\beta \right\}$$

where:

$$\Omega_r = \frac{T_{max}}{T_{th}}$$

$$T_{max} = \frac{2\, U_p\, (U_p + 2mc^2)}{Mc^2}$$

$$\beta = v/c = \left\{ 1 - \frac{1}{\left( \frac{U_p}{mc^2} + 1 \right)^2} \right\}^{1/2}$$

$U_p$ is the accelerating voltage (keV), $mc^2$ is the rest energy of the electron, $Mc^2$ is the rest energy of the nucleus, $\alpha$ is Z/137, Z is the atomic number, $U_R$ is the Rydberg constant (0.0136 keV), and $a_o$ is the Bohr radius (0.053 nm). The maximum energy that an incident electron can transfer to a nucleus is $T_{max}$. The minimum energy necessary to move an atom off its lattice site into some metastable position is $T_{th}$, which depends directly on the atomic number.

All materials undergo direct displacement of atoms above their specific threshold energy. For most metals the threshold energy is 20-30 eV (Makin, 1978) and therefore knock-on damage in the TEM does not occur when using accelerating voltages less than 300 keV. However for lighter elements such as Al (or Mg), direct displacement is observed at accelerating voltages below 200 keV (Makin, 1978).

Above the threshold energy for the knock-on process, the cross-section for knock-on increases with increasing accelerating voltage. The potential damage due to electron-nuclear interaction becomes more severe as the incoming electron gets more and more energetic. At higher accelerating voltages the electron has enough energy to cause multiple damage events. The quantity

$$N_d = \frac{T_{max}}{2\,T_{th}}$$

takes into account the possible cascade of damage events. The knock-on damage cross-section includes the cross-section for displacement of an atom directly due to interaction with the electron wave and the probability of being displaced by another "knocked" atom. The cross-section for knock-on damage increases with accelerating voltage as shown in figure 5.

### 2.1.2 Radiolytic damage

The relativistic cross-section for the interaction between the incident electron and the specimen electron is given by (Hobbs, 1979):

$$\sigma_e = \left( \frac{8 \pi a_o^2 U_R^2}{mc^2} \right) \left( \frac{Z}{T_{th}' \beta^2} \right)$$

where:

$$\beta = \left\{ 1 - \frac{1}{\left( \frac{U_p}{mc^2} + 1 \right)^2} \right\}^{1/2}$$

$T_{th}'$ is the minimum energy that must be transferred to the electrons of the solid to produce atomic nuclear movement, Z is the number of electrons (usually the atomic number) belonging to the target atom, $a_o$ is the Bohr radius (0.053 nm), $U_R$ is the Rydberg energy (13.6 eV), $U_p$ is the accelerating voltage and $mc^2$ is the rest energy of the electron($5.11 \times 10^5$ eV). The minimum energy $T_{th}'$ is specific to each unique atomic site within the specimen; it is related to the bond strength and the coordination number of the atom. The ionization cross-section consists of a constant, a "specimen specific" constant and a factor related to the inverse of the accelerating voltage,

$$\sigma_e = K \left( \frac{Z}{T_{th}'} \right) \beta^{-2}.$$

Thus the behavior of the cross-section for electronic interactions with accelerating voltage is determined by the parameter $\beta^{-2}$. This dependence is illustrated in figure 6 for the case of aluminum in zeolite Y. The cross-section for ionization decreases significantly with increasing accelerating voltage up to 500 keV, then levels off to a constant value.

The efficiency factor, $\varsigma$, for radiolysis in silicates is $10^{-4}$ (Hobbs, 1985). That is, for every ionization event that occurs, the probability of structural rearrangement is 0.0001. The cross-section for radiolytic damage is

$$\sigma_r = \sigma_e \times \varsigma.$$

Therefore the cross-sections for knock-on and radiolytic damage are of the same order of magnitude, and should both be considered when studying zeolites in the TEM especially when accelerating voltages above 200 keV are used. Above the knock-on threshold for Al, the damage rate for a zeolite will increase with accelerating voltage instead of decrease due to the increasing number of direct displacement events.

The effects of both radiolytic and knock-on damage events occurring simultaneously have been detected in synthetic quartz (Das and Mitchell, 1974); dislocation loops were attributed to direct atomic displacement, while the crystalline to amorphous transformation was considered to be the product of radiolysis. Generally when a material can undergo a radiolytic process, knock-on damage is insignificant. For example, in organic solids $\varsigma$ is $10^{-2}$ to $10^{-1}$ (Hobbs, 1985), yielding radiolytic damage cross-sections several orders of magnitude larger than the knock-on cross-sections, and direct atom displacement is not observed.

For alumino-silcates the cross-sections for knock-on and radiolytic damage predict that for an accelerating voltage below 200 keV, the damage should be due to a radiolytic process. The radiolytic cross-section can not, however, predict the actual structural relaxation responsible for the damage.

## 2.2 Experimental procedure

Samples of Y zeolite (with sodium cations) with Si/Al-ratios = 2.4, 18, $\infty$ were investigated. The samples were provided by I. Chan of Chevron Research Company. The powder samples were ground with an agate mortar and pestle and baked in an oven at 350°C for three hours to drive off residual water. Specimens for the TEM were prepared by embeddment in LR White acrylic resin, followed by thin sectioning (50-80nm) with a diamond knife on a Dupont-Sorvall MT-6000 microtome (Csencsits et al, 1985). The specimens were stored in a dessicator to reduce the readsorption of water. The accelerating voltage in the JEOL 200CX HREM was varied from 80-200 keV. Typically HREM micrographs are recorded with a current density of $\approx 10^{23} \frac{e}{s} m^{-2}$, however, to slow the degradation for these experiments lower current densities were used. For specimens with Si/Al-ratios = 2.4 and 18, the current density to the specimen was $1.57 \times 10^{22} \frac{e}{s} m^{-2}$. For specimens with Si/Al-ratios = $\infty$, the current density was $6.28 \times 10^{22} \frac{e}{s} m^{-2}$; damage at lower current density was too slow to observe within reasonable times. Incident beam current was measured at the image plane with an electrometer and the current density at the specimen was determined using $\phi_{specimen} = (Mag)^2 \phi_{image}$ ($\phi$=current density). This dependence was verified by measuring the current density at the image plane while maintaining a constant current density at the specimen. Over the magnification range 19,000 to 100,000, the measured current density varied inversely with the square of the magnification, to within the 10% uncertainty of the measurement.

The crystalline to amorphous transformation was monitored by recording on photographic film the loss of intensity in the Bragg reflections in the selected area diffraction (SAD) pattern with time. The SAD pattern was taken from a $5 \mu m^2$ region in the center

of a $20\mu m^2$ area of uniform current density. It is the long range periodicity of the crystalline solid that gives rise to strong intensity in the diffraction spots and as this long range periodicity is destroyed the intensity in the spots is reduced. Figures 7 and 8 show some representative diffraction data. The upper three micrographs in both figures show the loss of crystallinity in the initial 9 minutes under the electron beam. The lower three micrographs in figures 7 and 8 show the final stages of the transformation that took 21 minutes and 16.8 minutes, respectively, to complete. For each specimen at every accelerating voltage, the transformation was monitored several times to insure the reproducibility of the data. The dose to vitrification was calculated by multiplying the current density by the time to complete the phase transformation.

The measurement of current density was accurate to within 2% for all trials. For specimens with Si/Al-ratios = 2.4 and 18, the transformation time determinations had an uncertainty of $\approx$9%. This results in an uncertainty in the dose to vitrification of $\approx$9%. For specimens with Si/Al-ratio = $\infty$, the uncertainty in the transformation time was $\approx$12%, probably due to inhomogeneity in the crystals. The resulting uncertainty in the dose to vitrification is $\approx$12%.

**2.3 Results**

The metamict transformation took from 5 to 25 minutes to complete, depending on the Si/Al-ratio and the accelerating voltage. The dose to vitrification is plotted as a function of accelerating voltage for the three samples in figure 9. For all samples, increasing the accelerating voltage extends their crystalline lifetime. This indicates that the damage is radiolytic and that knock-on damage is not significant up to 200 keV. The difference between the dose to vitrification for the samples with Si/Al-ratios 2.4 and 18 is about 25%; for the sample with Si/Al =$\infty$, the dose to vitrification is 3.5 and 5

times greater than that for the samples with Si/Al-ratios 18 and 2.4, respectively. Total replacement of all the aluminum by silicon produces a zeolite that is significantly more stable to electron irradiation as well as to elevated temperatures.

Radiolytic degradation of $SiO_2$ in the TEM has been explained (Hobbs, 1979) as the weakening of Si-O bonds by the incorporation of $H_2O$ in the structure. Since zeolites are alumino-silicates where the aluminum occupies some of the tetrahedral positions of the silicon, the local structure is the same as $SiO_2$ (the Si (or Al) are tetrahedrally coordinated to four O), the radiolytic degradation mechanism could be the same. If this mechanism is applied to zeolites, the dependence of the rate of degradation on the amount of adsorbed water in the structure (Bursill et al, 1980) is explained. If this mechanism is responsible for degradation of zeolites then the increase in dose to vitrification with Si/Al-ratio should be explained by the different cross-sections for radiolytic damage for Si and Al in the zeolite structure. The ratio of the radiolytic cross-sections for an all Si containing zeolite versus an all Al containing zeolite is

$$\frac{\sigma_{Si}}{\sigma_{Al}}=0.80.$$

This predicts that a zeolite structure containing only aluminum atoms (all silicon atoms replaced with aluminum atoms) should degrade with a dose to vitrification 80% that for degradation of the same zeolite containing only silicon atoms (all aluminum atoms replaced with silicon atoms). This does not explain the data shown in figure 9 where the sample containing 29% Al (Si/Al=2.4) has a dose to vitrification 20% that of the Si/Al=$\infty$ sample.

The data in figure 9 indicates that the mechanism and therefore the efficiency of radiolytic damage in zeolites is different from that in quartz. The important difference

with aluminum in the structure is that each Al has a cation associated with it to balance the framework charge. This cation facilitates a different mechanism for degradation of aluminum-containing zeolites.

Figure 10 shows a model of a silicon atom tetrahedrally coordinated to four oxygen atoms in the zeolite structure. It is difficult to describe the damage mechanism for a silicon site in a zeolite. If only one Si-O bond is broken the Si atom is rigidly held in place by the three other existing Si-O bonds and the requirement that Si be tetrahedrally coordinated causes the broken Si-O bond to reform without any structural changes. When two Si-O bonds are broken, the Si atom is free to rotate about the two existing Si-O bonds and form bonds in a configuration different from the original structure, however, this leaves some bonds unsatisfied unless several other nearby tetrahedra are rotating and reforming bonds simultaneously.

Figure 11a shows the case of Al tetrahedrally coordinated to four oxygen atoms in the zeolite framework. If one Al-O bond is broken (fig. 11b), the Al can remain coordinated to only three oxygens and the cation can bond to the forth oxygen. The Al is stable with three bonds and the cation is still near it for local charge neutrality, but now the structure is permanently changed. The larger the cation the slower its movement into the proper position for bonding to the terminal oxygen and the higher the probability for reforming the original Al-O bond and preserving the structure.

### 2.4 Conclusions

Experimental evidence has confirmed the theoretical model for radiation damage of Y zeolites at low accelerating voltages in the transmission electron microscope. In the range 80-200 keV, the damage is radiolytic and using the highest accelerating voltage prolongs the lifetime of the zeolite.

A mechanism is proposed for radiolytic damage in zeolites. Structural relaxation is enhanced at Al sites due to the presence of a cation. When an Al-O bond is broken the cation moves into a position to bond to the dangling oxygen atom and the aluminum atom remains bound to only three oxygen atoms. Local charge neutrality is preserved, however, the structure is permanently changed.

This mechanism explains the damage rate dependence on the cation size (Bursill et al, 1981), Si/Al-ratio, as well as on the amount of adsorbed water in the structure (Bursill et al, 1980). At an aluminum site the larger the cation, the slower its movement into the proper position to bond to the dangling oxygen due to steric hindrance. Therefore at a given Si/Al-ratio the zeolite with the larger cations will be more stable than the same zeolite framework with smaller cations. As the Si/Al-ratio increases the number of possible degradation sites decreases and the zeolite is more stable to electron irradiation. The same trend should be observed if the number of cations in the structure is reduced by using cations with greater ionic charge; ie., $Ca^{2+}$ instead of $K^{+}$. This is the subject of future work. Adsorbed water in the zeolite structure can fill the role of a cation in the damage mechanism. Adsorbed water can bond to the dangling oxygen atom resulting in a structural change at either a Si or an Al site. Thus, dehydrating the zeolite will always enhance its stability under the electron beam regardless of the Si/Al-ratio or type of cation present.

# 3. COMPUTER IMAGE SIMULATION

## 3.1 Introduction

The effects of radiolytic damage of Y zeolites on their high resolution electron microscope images is investigated using computer simulation. The goal of this study is to determine how much of a specimen can be damaged without serious detrimental effects to the image.

The high resolution images are computed using the 81D version of the Simulated High Resolution Lattice Image (SHRLI) (O'Keefe and Buseck, 1979) programs running on the LBL VAX8600; the dynamical electron scattering calculation uses the multislice method (Goodman and Moodie, 1974). The SHRLI series is based on a 128 x 128 Fast Fourier transform and consists of four main programs: FCO128, PG128, MSF128 and IM128. The program FCO128 takes the atomic structural information (unit cell parameters, atomic positions and numbers, space group symmetry operators and temperature factors) and produces 2-dimensional Fourier coefficients of crystal potential for the Laue zone nearest the specified electron beam direction. These Fourier coefficients are output from FCO128 and together with user-specified "control data" (accelerating voltage of the microscope and the slice thickness of the phase-grating) are input to PG128 which produces single-slice dynamical scattering amplitudes. A number of these single-slice dynamical scattering amplitudes are input to the MSF128 program that calculates the electron wavefield diffracted from the crystal of selected thickness. The program IM128 uses the output from MSF128 and microscope specific "control data" (coefficient of spherical aberration, spread of focus halfwidth, beam convergence, objective lens focus and objective aperture size and placement) to produce images of the crystal at various thicknesses and focus settings.

### 3.2 Computations

Images were simulated for Y zeolite oriented with the electron beam down the [110] zone axis parallel to the channels. The atomic coordinates of Y zeolite were taken from work by Baur (1964). To reduce the computation time, and since the difference in the scattering potential between Al and Si is negligible, the structural model used for Y zeolite was a framework consisting of silicon and oxygen atoms without cations or water molecules.

To simulate damage in the crystal an amorphous computational cell was created by randomization of the atoms in Y zeolite (appendix). Half of the 192 Si were kept tetrahedrally coordinated to four oxygen atoms; these tetrahedral units ($SiO_4$) were randomly oriented and placed in a cube with edge length equal to 2.474nm. The remaining 96 Si atoms were randomly placed in the remaining empty space in the cube. Placement of all atoms was such that the interatomic distance between atoms was at least as large as their interatomic spacing in zeolite Y (Smith, 1976).

Dynamical electron scattering is used to simulate HREM images; the interactions of all diffracted beams enter into the calculations to produce the final electron wavefield at the bottom of the crystal. The number of diffracted beams used in the calculations must be sufficiently large to account for this dynamical scattering. For these computations 2267 diffracted beams were propagated through the crystal. In order to do this, interactions were considered with 9089 phase-grating coefficients out to 25.85nm$^{-1}$. For accurate representation of the phase-grating by the 128 x 128 array (Self et al, 1983), the slice thickness was 0.4998nm.

Images were computed for JEOL 200CX electron microscope (EM) parameters; viz, spherical aberration coefficient of 1.2mm, spread of focus halfwidth of 10nm, beam con-

vergence of 0.5mrad; the objective aperture corresponded to 5.0nm$^{-1}$ and admitted 350 diffracted beams. The maximum specimen thickness assumed was 60 nm; in general a good microtomed thin section is 45-60 nm thick.

### 3.3 Results

Figure 12 shows the projected potential map of the Y zeolite unit cell and the amorphous computational unit cell in the [110] projection. This is how the image would look using an ideal microscope with infinite resolution. In the projected potential map of Y zeolite the large (≈0.74nm) and the small (≈0.22nm) tunnels are seen clearly. The projected potential map of the amorphous cell does not show any periodicities or ordering; the structure is random.

Simulations of the HREM images of perfect Y zeolite (fig. 13, 100% perfect) at Scherzer defocus (Scherzer, 1949) (-60nm for the 200CX EM) reveal that only for a specimen up to 20nm thick would the image be close to a structure image (Cowley, 1976). In a structure image the details in the image correspond directly to features in the specimen; ie., dark areas represent a high potential, many atoms, whereas light areas correspond to few or zero atoms. A true structure image would look very much like the projected potential map viewed at the resolution of the microscope. The HREM images of the 100% perfect Y zeolite at thicknesses 10-20nm are not truly structure images because there are gray patches in the large tunnels in the images. This anomalous dark contrast is due to the contrast-transfer-function (CTF) (Frank, 1973) for the 200CX electron microscope. Figure 14 shows that the lowest frequency reflection from Y zeolite ($(1\bar{1}1)$ in the [110] orientation) is largely blocked by phase shifts in the objective lens of the microscope at -60nm defocus. Only approximately 21% of the amplitude of the $\{111\}$ reflection is passed to contribute to the image, and it is this missing frequency

that produces the dark contrast at the tunnel positions (Chan, et al, 1986).

For specimen thickness greater than 20nm at Scherzer defocus, the computer HREM images contain additional non-structural detail (fig. 13, 100% perfect). This non-structural detail results from second order interferences of the dynamically scattered electron waves (O'Keefe, 1979). Since most microtomed thin sections are 50-60nm thick, their electron microscope images should not be interpreted intuitively because their images will bear little or no direct resemblance to their projected potential.

Figures 15 through 18 (100% perfect) show the effects of larger values of defocus on the HREM images of Y zeolite. As the microscope is defocused beyond Scherzer defocus, the image detail can not be related to the structure except for the white areas corresponding to the large channels. The large channels are visible at larger defocus values because the CTF changes shape and allows more of the amplitude of the {111} reflection to contribute to the image.

The effects of damage on HREM images of Y zeolite are visible in figures 13 and 15 through 18. The most obvious effect in the image for a specific thickness and defocus is a continuous loss of image contrast and sharpness with the loss of crystallinity. At Scherzer defocus (fig. 13) for a specimen with 60% perfect Y zeolite at a thickness 30nm or greater, the images have become fuzzy shades of grey without any discernible detail. This loss of detail with increased damage occurs for all choices of specimen thickness and microscope defocus.

In some cases the loss of detail in the image due to vitrification can be an advantage, particularly when the details are not related to the structure. A thick crystal (60nm) at a large defocus (-100nm), with 70-50% of its thickness perfect (fig. 16), produces an image which can be related to the structure. These images are similar to the

images of thin crystals of 100% perfect Y zeolite at optimum defocus (fig. 13, $\leq$20nm); both the large and small channels are visible. This is in contrast to the 60nm thick crystal with 70-50% perfect crystal at Scherzer defocus (-60nm) which shows non-structural detail, as does a 60nm-thick 100% perfect crystal. In thick crystals at large defocus values, the amorphous damage in the specimen reduces the visibility of the non-structural detail and produces HREM images that provide information about the structure.

### 3.4 Conclusions

Image simulation has shown that only under very specific conditions are HREM images of Y zeolite structure images. These specific conditions are not usually met under normal experimental conditions. The limitation of specimen thickness may perhaps be reduced by ion-thinning of the microtomed thin sections. A reduction in specimen thickness will decrease the non-structural details in the HREM images which are due to second order dynamical interactions of the electron waves.

Although a structure image can not be produced, information about the microstructure can be obtained by taking a series of micrographs of a thin specimen, at various values of underfocus. Near Scherzer defocus, the structural details of the small tunnels are observed in the HREM image, while at greater values of underfocus the large tunnels are visible. By comparison of several images with computer simulated images, the correct microstructure can be determined.

The damage of Y zeolites generally results in a decrease in the contrast and the sharpness of the details in HREM images. If a crystal has less than 20% of its thickness amorphous, its HREM images are not significantly different from those of a perfect crystal and image interpretation is unchanged. As a specimen becomes more and more

damaged there is a loss of detail in the image that can in some cases be serendipitous. At large defocus values (-100nm), thick crystals (60nm) with 30-50% of their thickness amorphous, produce HREM images which can be related to the structure because the presence of the amorphous material decreases the visibility of non-structural detail. This reduction in visibility of non-structural details can aid the interpretation of the images.

## APPENDIX: CONSTRUCTION OF COMPUTATIONAL CELL

An amorphous computational cell is created by placing the 576 atoms of Y zeolite in a cube with edge length equal to 2.474nm. In order to preserve as much of the proper coordination of the $Si^{4+}$ as possible, half of the silicon atoms are tetrahedrally coordinated to four oxygen atoms; these $SiO_4$ units are randomly rotated and randomly placed in the cube. The other 96 Si atoms are then randomly placed in the remaining cube volume. The interatomic distances are checked to be at least as large as the interatomic spacings in Y zeolite.

```
C     This program generates a random computational
C       unit cell of Y zeolite.
C
C
      Real*4 x(4),y(4),z(4),sx(96),sy(96),sz(96)
      Real*4 xr(4),yr(4),zr(4),six(96),siy(96),siz(96)
      Real*4 oxx(4,96),oxy(4,96),oxz(4,96)
      Integer*2 Flag,iseed,jseed,si,ox
C
C     Set coordinates for tetrahedral oxygen
C
      Data x/-0.0378054,0.0378054,-0.0378054,0.0378054/
      Data y/-0.0378054,0.0378054,0.0378054,-0.0378054/
      Data z/-0.0378054,-0.0378054,0.0378054,0.0378054/
C
C     Accept seeds for random number generator
C
      type 5
    5 FORMAT(' ENTER SEEDS: '$)
      ACCEPT 8,iseed,jseed
    8 FORMAT(2I8)
C
C     Set atomic parameters
C
      oc=1.0000000
      si=14
      ox=8
      temp=1.2
      tem2=2.65
```

```
      ucp=24.74
      chkO=2.65
      chkSO=1.62
      chkS=3.09
      ntet=96
      pi=3.1415927
      J=1
C
C     Choose random angle of rotation of tetrahedron
C
 30   alpha=2*pi*ran(iseed,jseed)
      beta=pi*ran(iseed,jseed)
      gamma=2*pi*ran(iseed,jseed)
      csa=cos(alpha)
      sna=sin(alpha)
      csb=cos(beta)
      snb=sin(beta)
      csg=cos(gamma)
      sng=sin(gamma)
      L=0
C
C     Rotate the tetrahedron
C
      Do 50 I=1,4
      xr(I)=(csa*csg-sna*csb*sng)*x(I)+(csa*sng+sna*csb*csg)*y(I)+
     *(sna*snb)*z(I)
      yr(I)=(-sna*csg-csa*csb*sng)*x(I)+(-sna*sng+csa*csb*csg)*y(I)+
     *(csa*snb)*z(I)
      zr(I)=(snb*sng)*x(I)+(-snb*csg)*y(I)+csb*z(I)
 50   continue
C
C     Choose random coordinates for Si
C
 60   L=L+1
      six(J)=ran(iseed,jseed)
      siy(J)=ran(iseed,jseed)
      siz(J)=ran(iseed,jseed)
C
C     Adjust coordinates of the tetrahedral O
C
      Do 70 I=1,4
      oxx(I,J)=amod(xr(I)+six(J)+1.0,1.0)
      oxy(I,J)=amod(yr(I)+siy(J)+1.0,1.0)
      oxz(I,J)=amod(zr(I)+siz(J)+1.0,1.0)
 70   continue
      if(J.EQ.1) goto 160
      FLAG=0
C
C     Si-Si interatomic distance check
```

```
C
      Do 90 N=1,J-1
      if(FLAG.EQ.1) goto 90
      dsts=sqrt((six(J)-six(N))**2+(siy(J)-siy(N))**2+
     *(siz(J)-siz(N))**2)
      dsts=dsts*ucp
      if(dsts.LT.chkS) FLAG=1
   90 continue
      if(FLAG.EQ.1) goto 60
C
C     O-O interatomic distance check
C
      Do 120 I=1,4
      if(FLAG.EQ.1) goto 120
      Do 110 N=1,J-1
      if(FLAG.EQ.1) goto 110
      Do 100 K=1,4
      if(FLAG.EQ.1) goto 100
      dsto=sqrt((oxx(I,J)-oxx(K,N))**2+(oxy(I,J)-oxy(K,N))**2+
     *(oxz(I,J)-oxz(K,N))**2)
      dsto=dsto*ucp
      if(dsto.LT.chkO) FLAG=1
  100 continue
  110 continue
  120 continue
      if(FLAG.EQ.1) goto 60
C
C     Si-O interatomic distance check
C
      Do 150 N=1,J-1
      if(FLAG.EQ.1) goto 150
      Do 140 K=1,4
      if(FLAG.EQ.1) goto 140
      dstso=sqrt((six(J)-oxx(K,N))**2+(siy(J)-oxy(K,N))**2+
     *(siz(J)-oxz(K,N))**2)
      dstso=dstso*ucp
      if(dstso.LT.chkSO) FLAG=1
  140 continue
  150 continue
      if(FLAG.EQ.1) goto 60
  160 J=J+1
      type 161,J
  161 FORMAT (' Tet=', I8)
      if(J.LE.ntet) goto 30
C
C     Now add in the other 96 Si
C
      L=0
      K=1
```

```
C
C     Choose random coordinates for Si
C
 170  L=L+1
      if(L/10*10.EQ.L) type 173,L
 173  FORMAT (' T=', I8)
 175  sx(K)=ran(iseed,jseed)
      sy(K)=ran(iseed,jseed)
      sz(K)=ran(iseed,jseed)
C
C     Si-Si interatomic distance check with tetSi
C
      FLAG=0
      Do 190 N=1,96
      if(FLAG.EQ.1) goto 190
      dsts=sqrt((sx(K)-six(N))**2+(sy(K)-siy(N))**2+
     *(sz(K)-siz(N))**2)
      dsts=dsts*ucp
      if(dsts.LT.chkS) FLAG=1
 190  continue
      if(FLAG.EQ.1) goto 170
C
C     Si-Si interatomic distance check with other single Si
C
      if(K.EQ.1) goto 255
      Do 195 N=1,K-1
      if(FLAG.EQ.1) goto 195
      dsts=sqrt((sx(K)-sx(N))**2+(sy(K)-sy(N))**2+
     *(sz(K)-sz(N))**2)
      dsts=dsts*ucp
      if(dsts.LT.chkS) FLAG=1
 195  continue
      if(FLAG.EQ.1) goto 170
C
C     Si-O interatomic distance check
C
      Do 250 N=1,96
      if(FLAG.EQ.1) goto 250
      Do 240 J=1,4
      if(FLAG.EQ.1) goto 240
      dstso=sqrt((sx(K)-oxx(J,N))**2+(sy(K)-oxy(J,N))**2+
     *(sz(K)-oxz(J,N))**2)
      dstso=dstso*ucp
      if(dstso.LT.chkSO) FLAG=1
 240  continue
 250  continue
      if(FLAG.EQ.1) goto 170
 255  K=K+1
      L=0
```

```
      if(K.LE.ntet) go to 175
C
C     Write random computational cell
C     parameters to atom position file.
C
      OPEN(unit=4,file='ranuc.at',access='sequential',status='new')
      WRITE(4,360)(J,si,oc,six(J),siy(J),siz(J),temp,(I,J,ox,oc,
     *oxx(I,J),oxy(I,J),oxz(I,J),tem2,I=1,4),J=1,ntet)
  360 FORMAT(96('Si',i2,2x,i2,F12.7,4F10.7,/
     *4('O',I1,I2,2x,i2,F12.7,4F10.7/)))
      WRITE(4,370)(K+96,si,oc,sx(K),sy(K),sz(K),temp,K=1,ntet)
  370 FORMAT(96('S',I3,x,i2,F12.7,4F10.7/))
      STOP
      END
C     By R. Csencsits, 11/18/85
```

## REFERENCES

Baur,W.H., Amer. Mineralogist **49** (1964) 698.

Beyer,H.K., and Belenykaja,I., "Catalysis by Zeolites", Studies in Surface Science and Catalysis 5, Elsevier, Amsterdam, 1980, p.203.

Bibby,D.M., Milestone,N.B., Patterson,J.E., and Aldridge,L.P., J. Catal. **97** (1986) 493.

Breck,D.W., "Zeolite Molecular Sieves", John Wiley & Sons, New York, 1974, p.92.

Bursill,L.A., Lodge,E.A., and Thomas,J.M., Nature **286** (1980) 111.

Bursill,L.A., Thomas,J.M., and Rao,K.J., Nature **289** (1981) 157.

Castellan, G.,"Physical Chemistry", Addison-Wesley, Massachusetts, 1971, p.762.

Chan,I.Y., personal communication, (1984).

Chan,I.Y., Csencsits,R., O'Keefe,M.A., and Gronsky,R., submitted for publication to J. Catal.

Cowley,J.M., Ann. Rev. of Mat. Sci. **6** (1976) 53.

Csencsits,R., Schooley,C., and Gronsky,R., J. Elect. Micros. Tech. **2** (1985) 643.

Das,G., and Mitchell,T.E., Rad. Effects **23** (1974) 49.

Fraissard,J.,"Catalysis by Zeolites", Studies in Surface Science and Catalysis 5, Elsevier, Amsterdam, 1980, p.343.

Frank,J., Optik **38** (1973) 519.

Goodman,P., and Moodie,A.F., Acta. Cryst. **A30** (1974) 280.

Hobbs,L.W., EMSA Bulletin **15** (1985) 51.

Hobbs,L.W., Introduction to Analytical Electron Microscopy, ed. J.J. Hren, J.I. Goldstein and D.C. Joy, Plenum press, New York, 1979, 437.

Klinowski,J., Thomas,J.M., Audier,M., Vasudevan,S., Fyfe,C.A., and Hartmann,J.S., J. Chem. Soc., Chem. Commun. (1981) 570.

Lechert,H., "Structure and Reactivity of Modified Zeolites", Studies in Surface Science and Catalysis 18, Elsevier, Amsterdam, 1984, p.107.

Makin,M.J., Ninth Int. Cong. On Elect. Micros. III (1978) 330.

McKinley,W.A. and Feshbach,H., Phys. Rev. **74** (1948) 1759.

Meier,W.H., and Olsen,D.H., Adv. Chem. Ser. **101** (1971) 155.

Miale,J.N., Chen,N.Y., and Weisz,P.B., J. Catal. **6** (1966) 278.

O'Keefe,M.A., Proc. 37th Ann. EMSA Meeting (1979) 556.

O'Keefe,M.A., and Buseck,P.R., Trans. Amer. Crystallogr. Asso. **15** (1979) 27.

Pabst,A., Amer. Mineralogist **37** (1952) 137.

Poutsma,M.L., in ACS Monograph 171,"Zeolite Chemistry and Catalysis", (J.A. Rabo,ed.), ACS, Washington, D.C., 1976; p.450.

Scherzer,O., J. Appl. Phys. **20** (1949) 20.

Seitz,F., and Koehler,J.S., Solid State Physics **2** (1956) 305.

Self,P.G., O'Keefe,M.A., Buseck,P.R., and Spargo, A.E.C., Ultramicroscopy **11** (1983) 35.

Smith,J.V.,in ACS Monograph 171,"Zeolite Chemistry and Catalysis", (J. A. Rabo,ed.), ACS, Washington, D.C., 1976; p.17,49.

Thomas,J.M., and Millward,R., J. Chem. Soc., Chem. Commun. (1982) 1380.

Thomas,J.M., Ramdas,S., and Millward,R., New Scientist **18** (1982) 435.

## FIGURE CAPTIONS

1. A stereodiagram of the alumino-silicate framework structure for zeolite Y and faujasite (after Smith,1976).

2. The sodalite cage structure. A tetrahedral atom (Si, Al) is at each vertex; there are six square faces (4-membered rings) and eight hexagonal faces (6-membered rings).

3. Structure of faujasite-type zeolites. Hexagonal prisms join the sodalite cages creating large channels.

4. TEM image of zeolite Y, the arrows mark the damage areas.

5. Knock-on cross-section versus accelerating voltage for Al in Y zeolite.

6. Radiolytic cross-section versus accelerating voltage for Al in Y zeolite.

7. Fading of diffraction spots over 21 minutes at 200 keV for sample Si/Al=18.

8. Fading of diffraction spots over 16.8 minutes at 200 keV for sample Si/Al=$\infty$.

9. Dose to vitrification versus accelerating voltage for Y zeolites with Si/Al = 2.4, 18, $\infty$.

10. Silicon atom tetrahedrally coordinated to four oxygen atoms in the zeolite structure.

11a. Aluminum atom tetrahedrally coordinated to four oxygen atoms in the zeolite structure.
11b. Aluminum atom coordinated to three oxygen atoms in the damaged zeolite structure.

12. Projected potential map [110] for Y zeolite unit cell and the amorphous computational unit cell.

13. Computer simulated HREM images at Scherzer defocus (-60 nm) of 100%-50% perfect Y zeolite.

14. Contrast-transfer-function for the 200CX microscope at Scherzer (-60 nm).

15. Computer simulated HREM images of 100%-50% perfect Y zeolite at -80 nm defocus.

16. Computer simulated HREM images of 100%-50% perfect Y zeolite at -100 nm defocus.

17. Computer simulated HREM images of 100%-50% perfect Y zeolite at -120 nm defocus.

18. Computer simulated HREM images of 100%-50% perfect Y zeolite at -140 nm defocus.

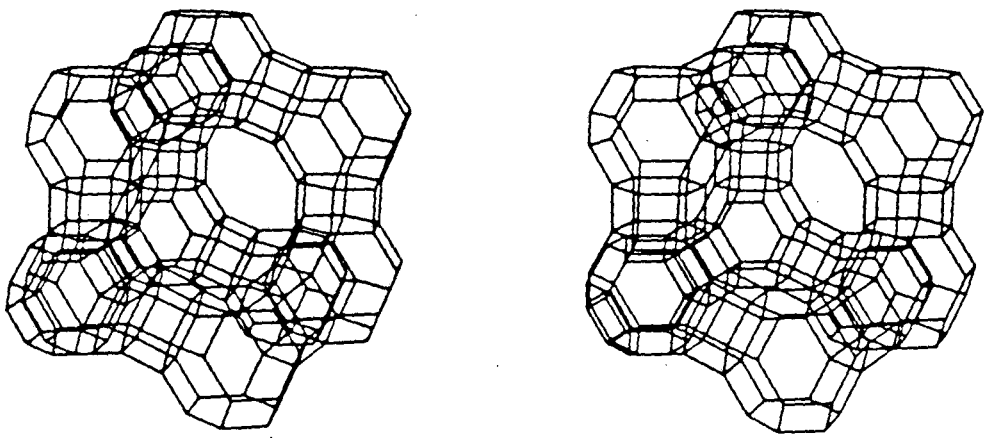

Fig. 1

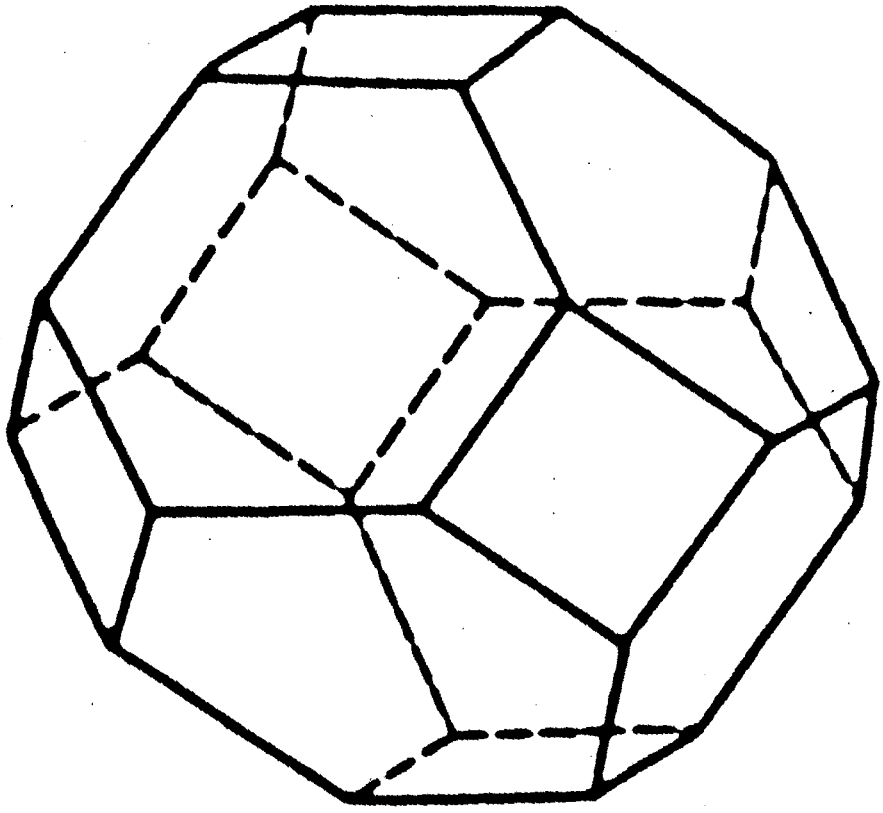

XBL 861-338

Fig. 2

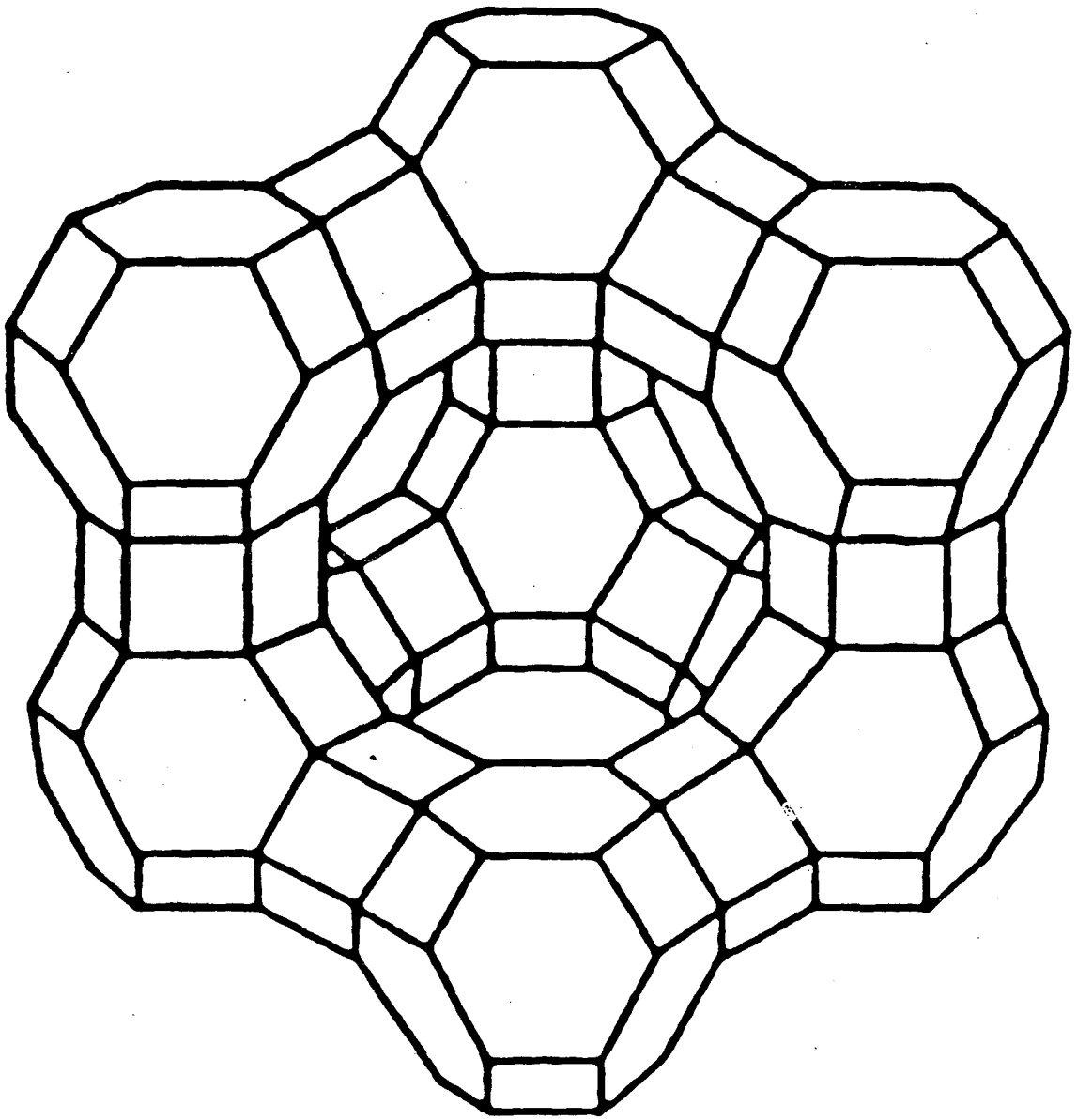

XBL 861-337

Fig. 3

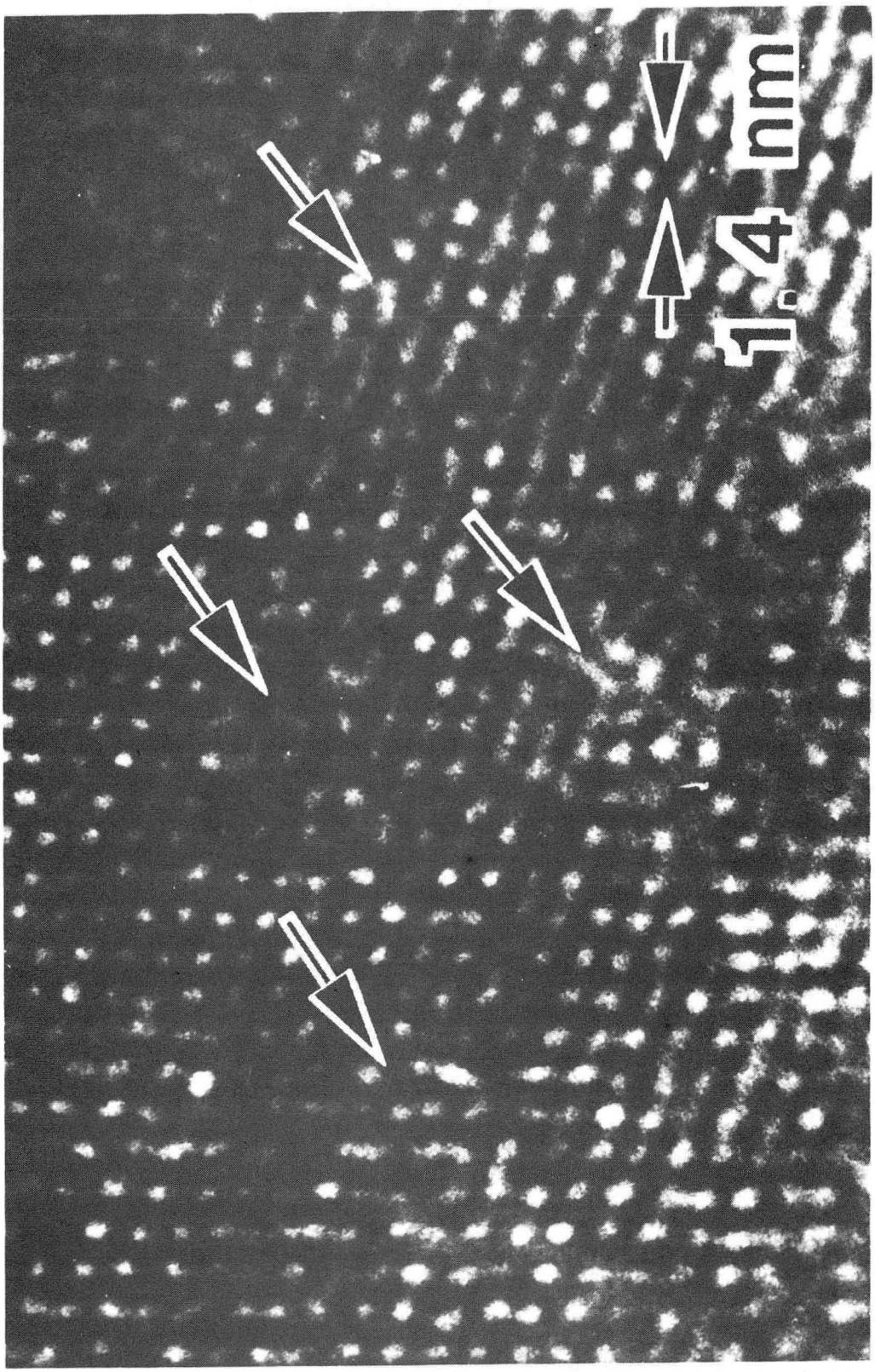


XBB 856-4514

Fig. 4

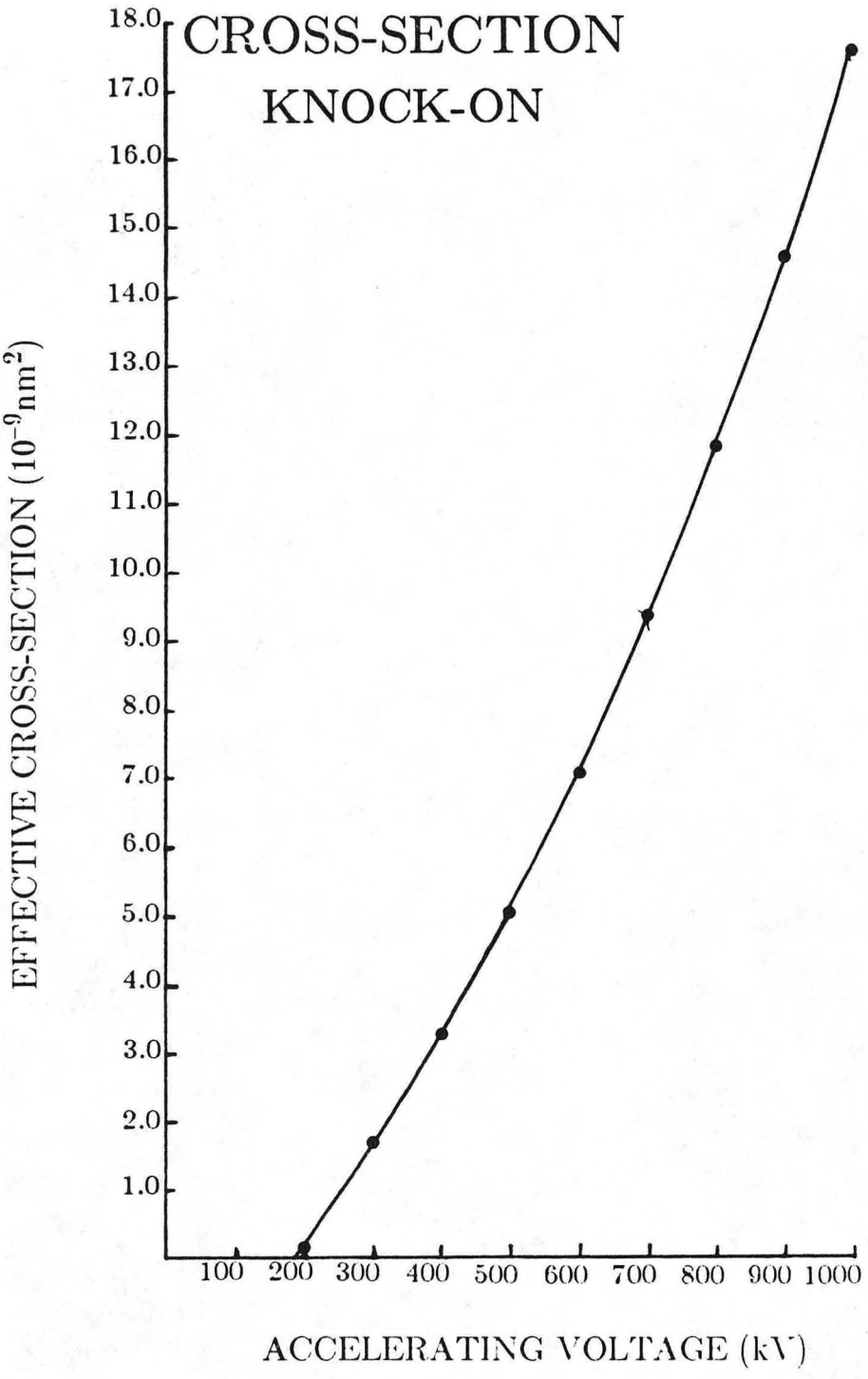


XBL 8511-4566

Fig. 5

# RADIOLYTIC CROSS-SECTION

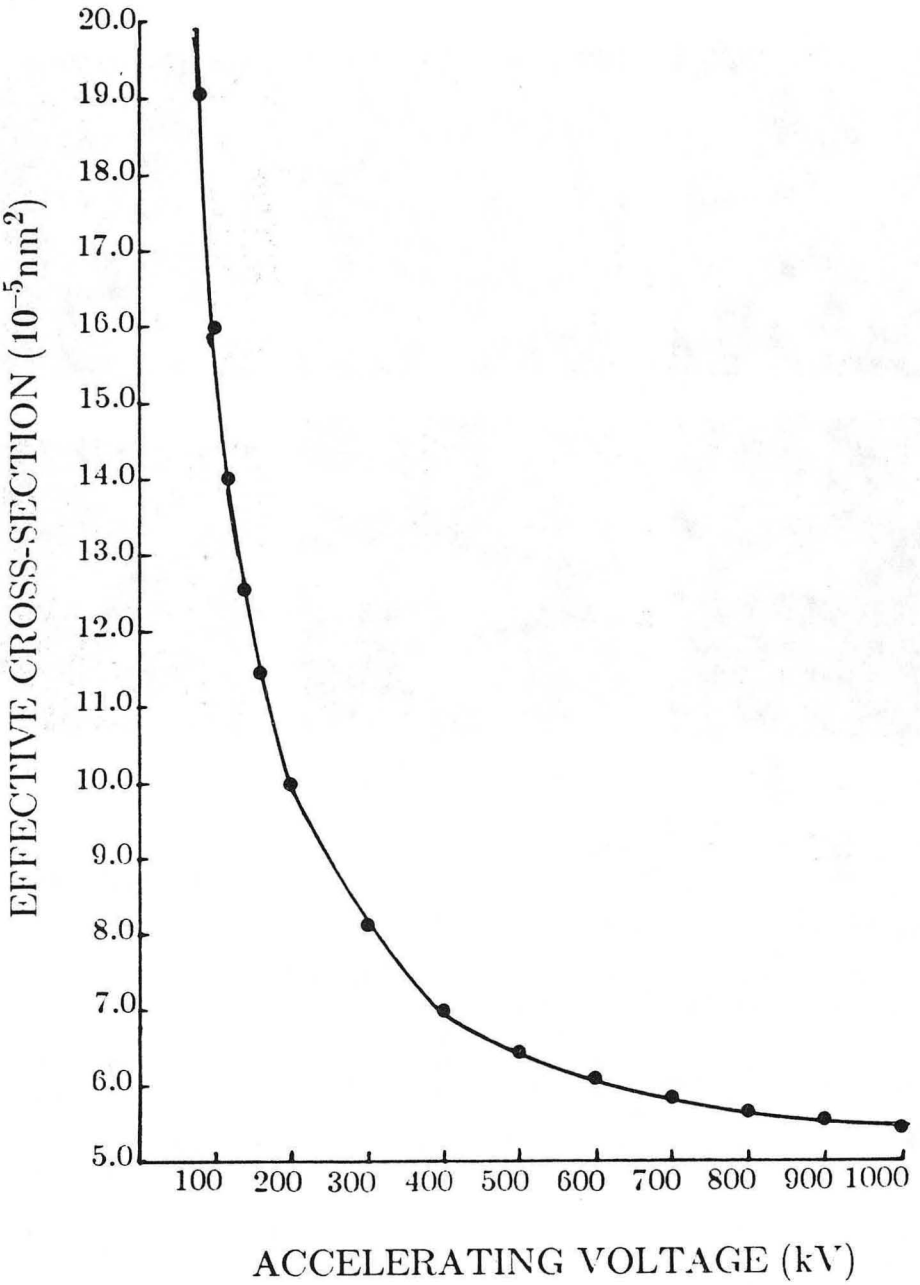


XBL 8511-4565

Fig. 6

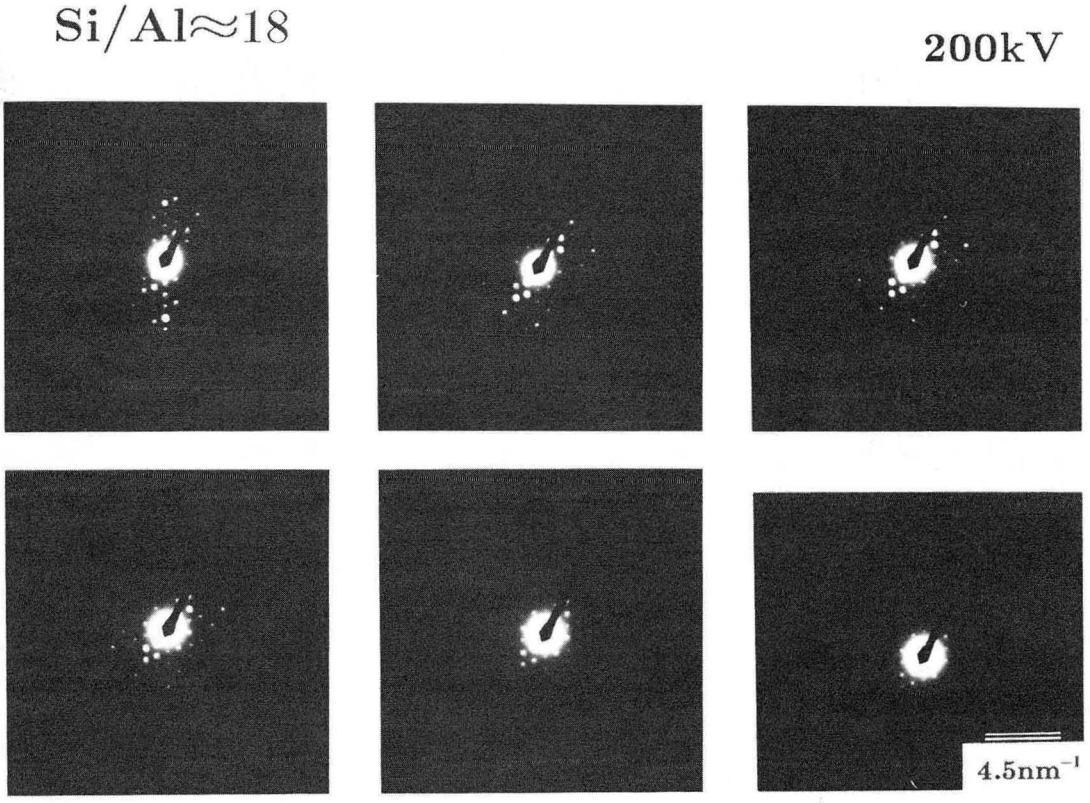
Si/Al≈18
200kV
4.5nm⁻¹
21m
$\phi = 1.57 \times 10^{22} \frac{e}{s} m^{-2}$
XBB 850-8304

Fig. 7

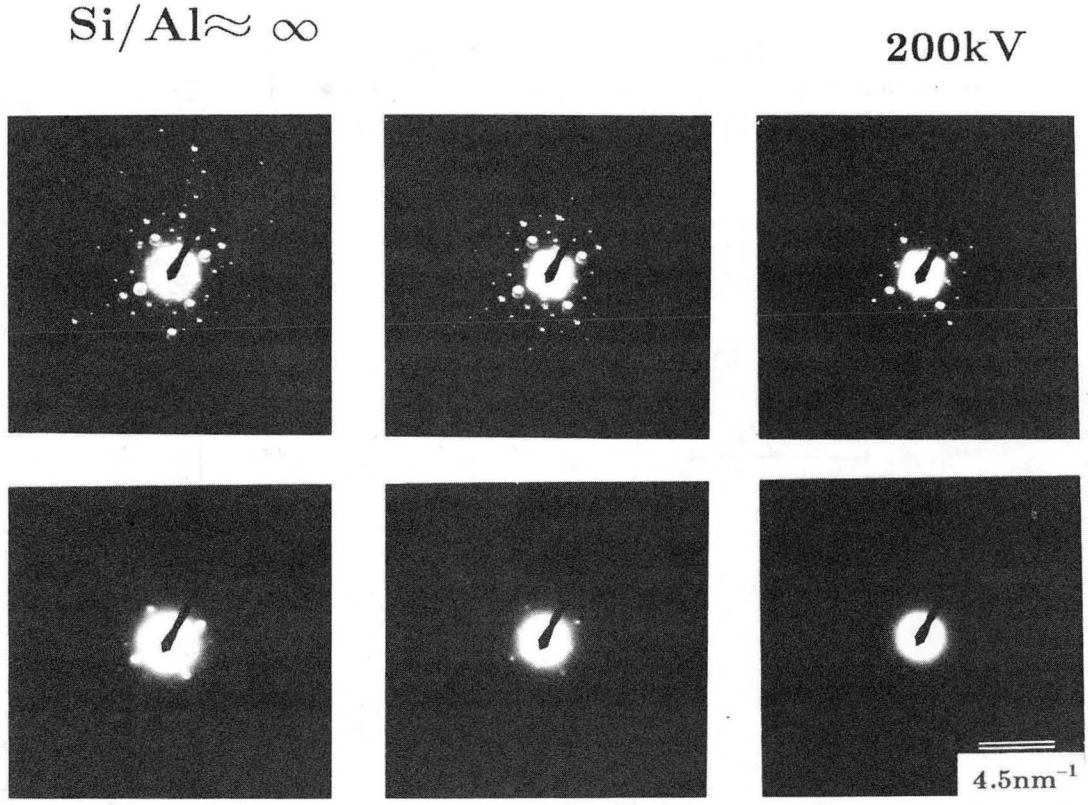
Si/Al≈ ∞
200kV
4.5nm$^{-1}$
16.8m
$\phi = 6.28 \times 10^{22} \frac{e}{s} m^{-2}$
XBB 850-8309

Fig. 8

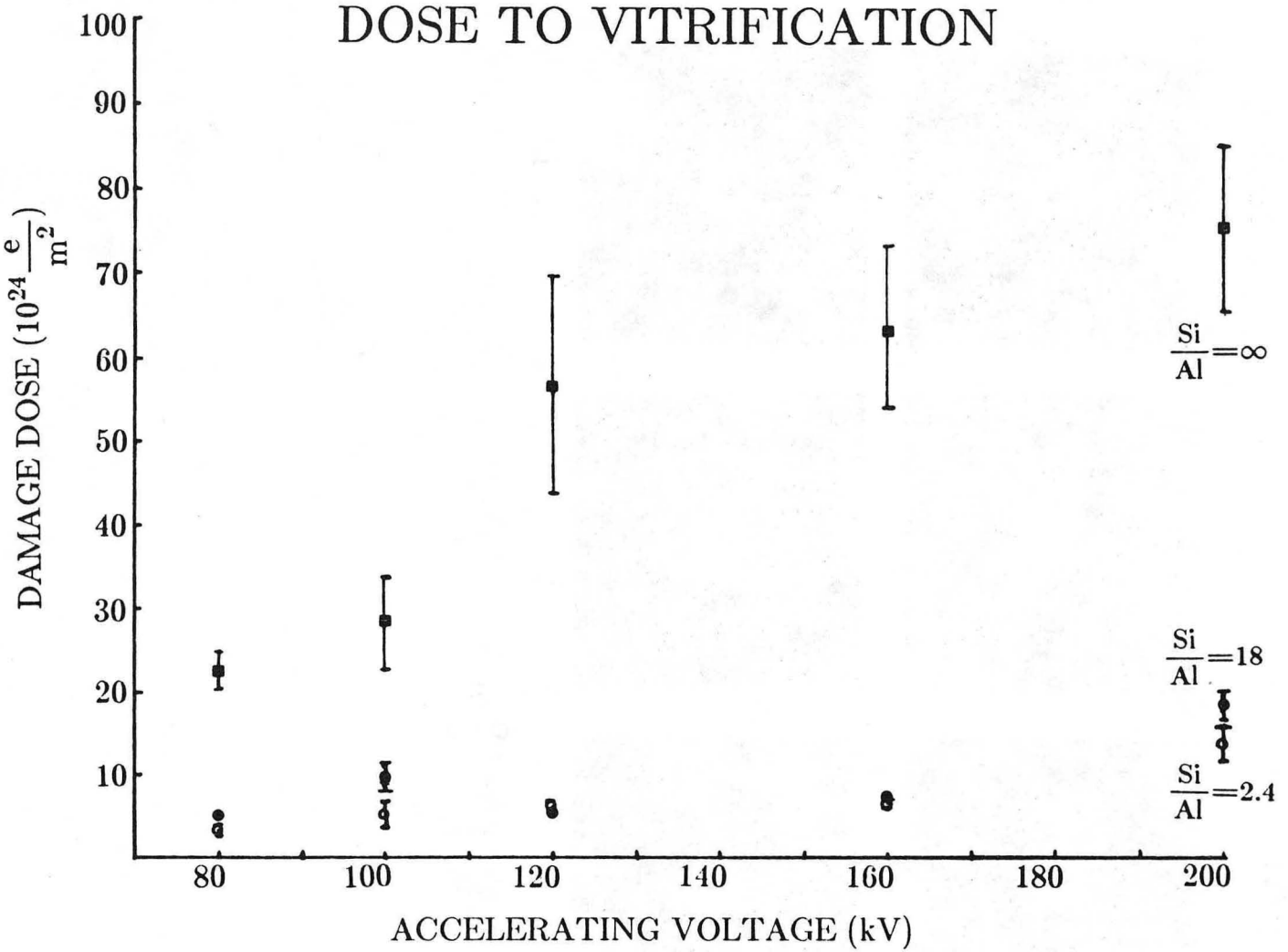


Fig. 9

XBL 8511-4567

# Tetrahedral Si in zeolite structure

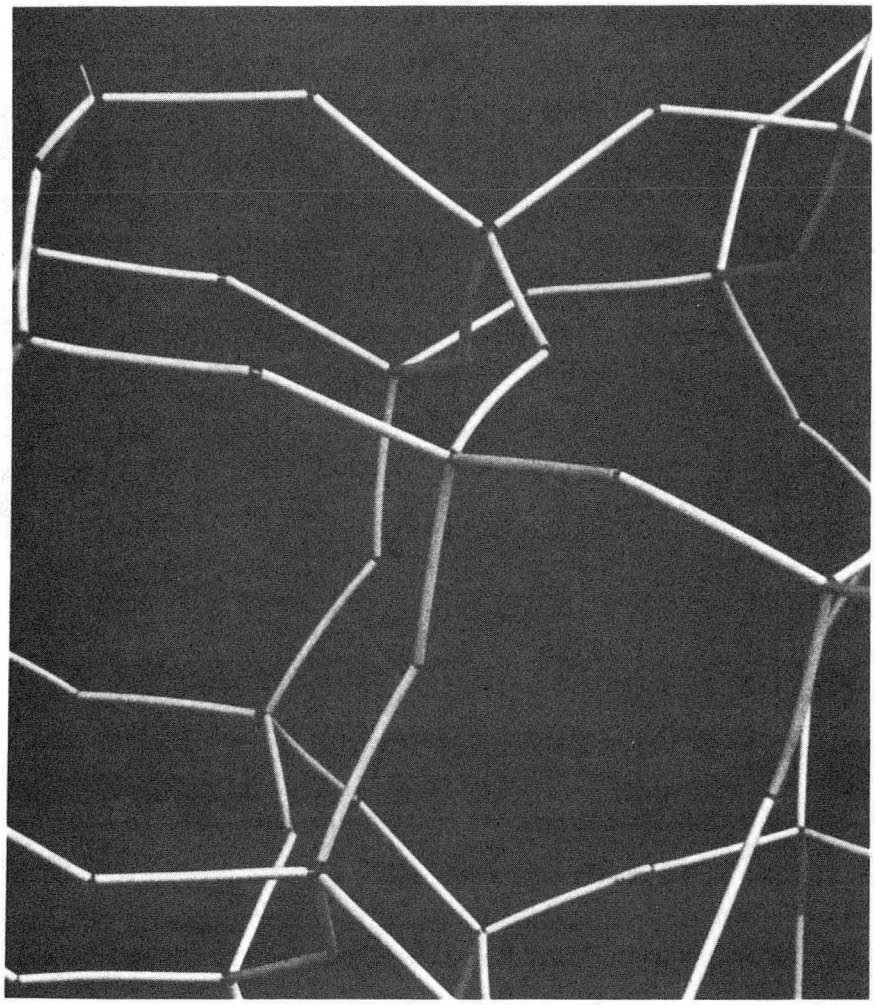

XBB 850-9268

Fig. 10

# Al-CATION DAMAGE MECHANISM

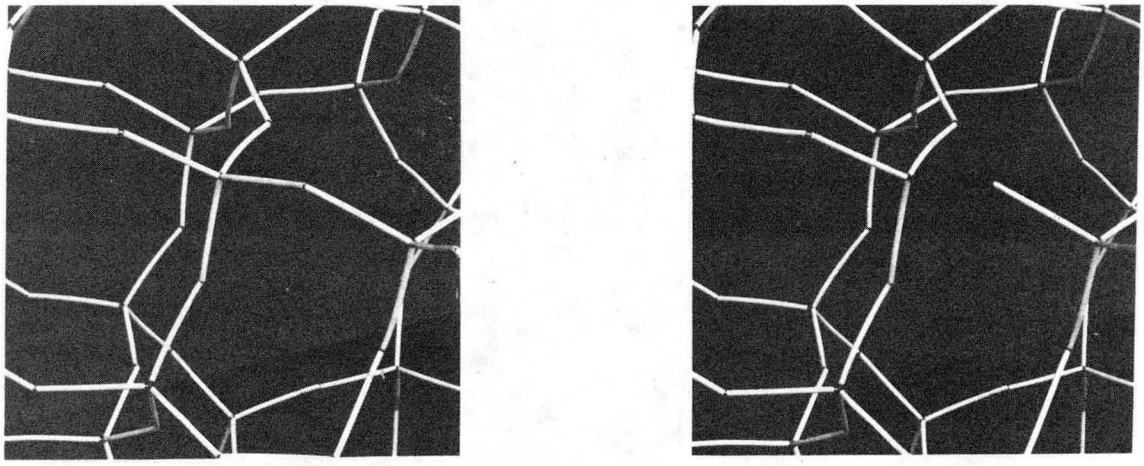

Al: 3 coordinated

Cation: more tightly bound

XBB 850-9269

Fig. 11

# Projected Potential [110]

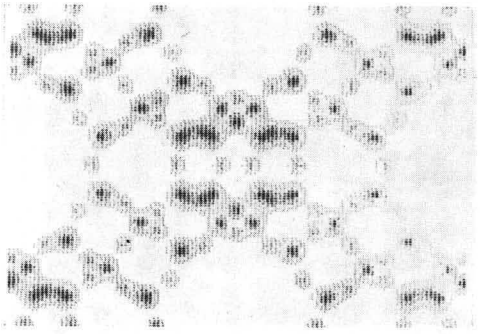

Y-Zeolite

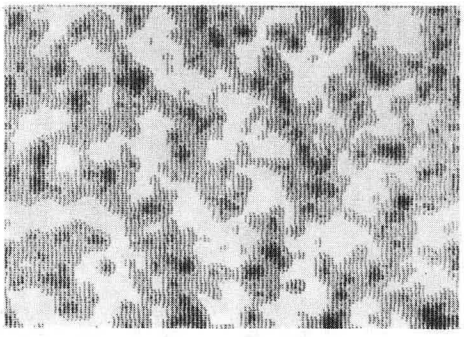

Amorphous

XBB 850-9649

Fig. 12

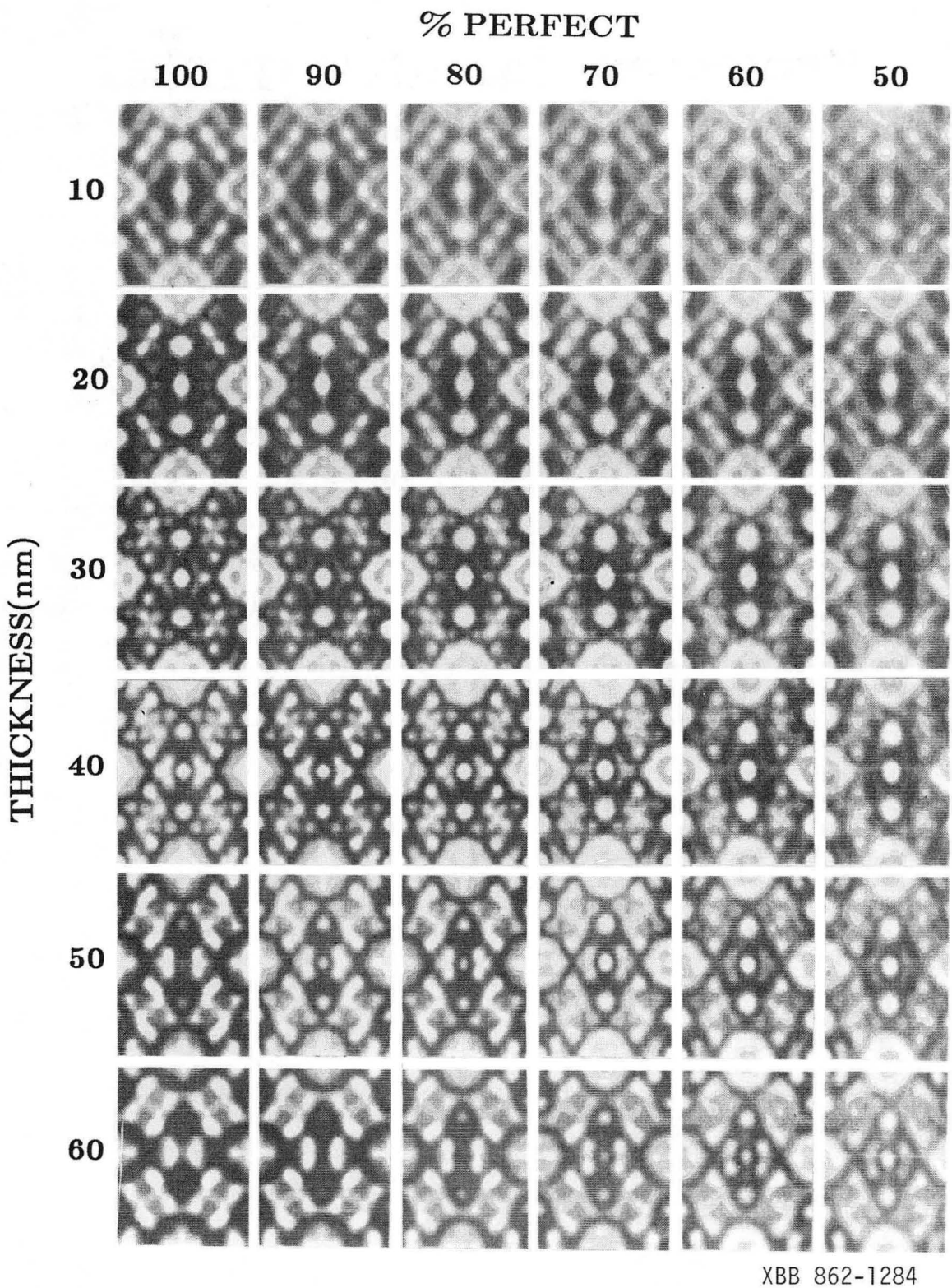
Δf=-60nm
% PERFECT
100
90
80
70
60
50
THICKNESS(nm)
10
20
30
40
50
60
XBB 862-1284

Fig. 13

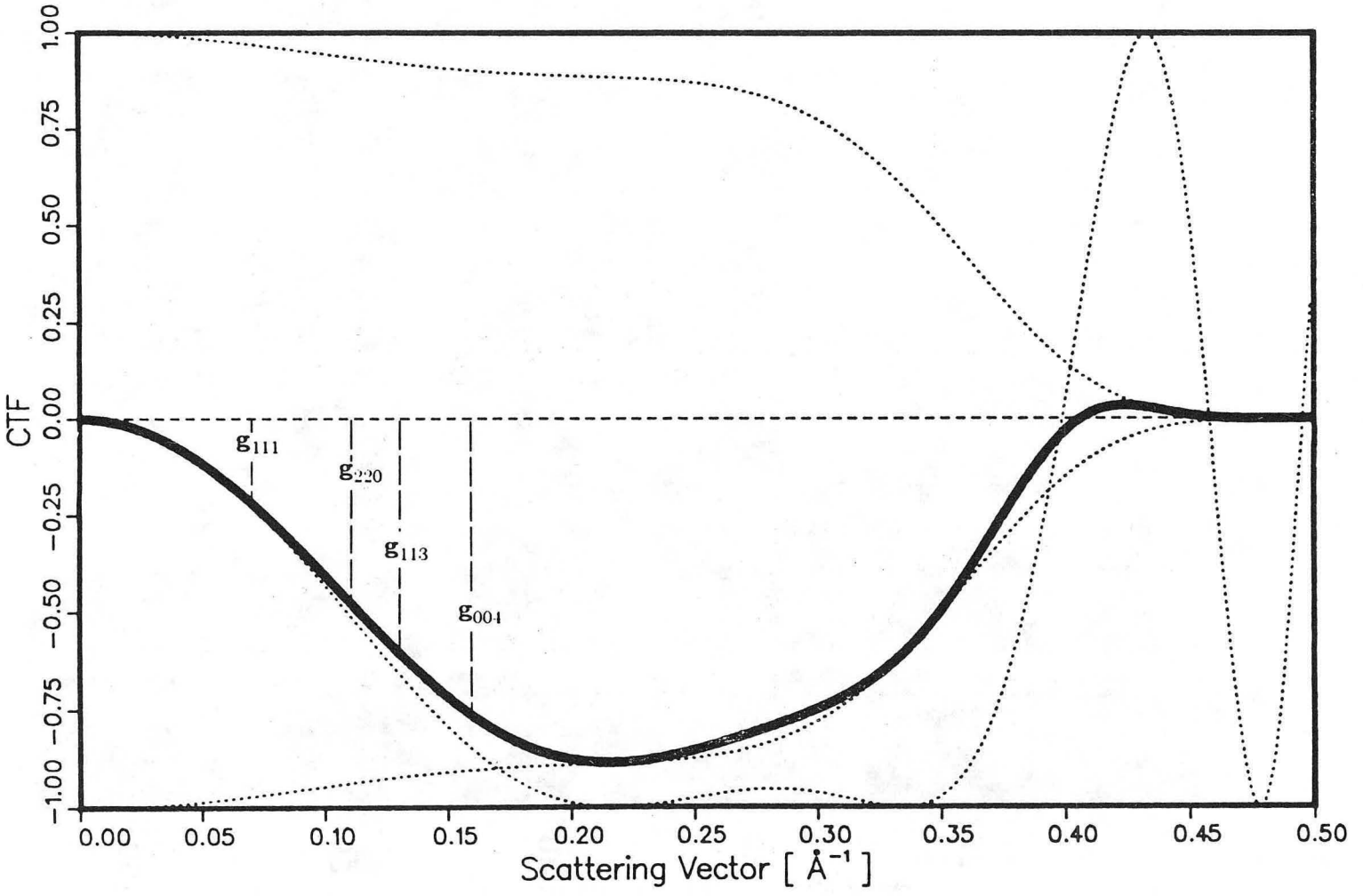


XBL 862-430

Fig. 14

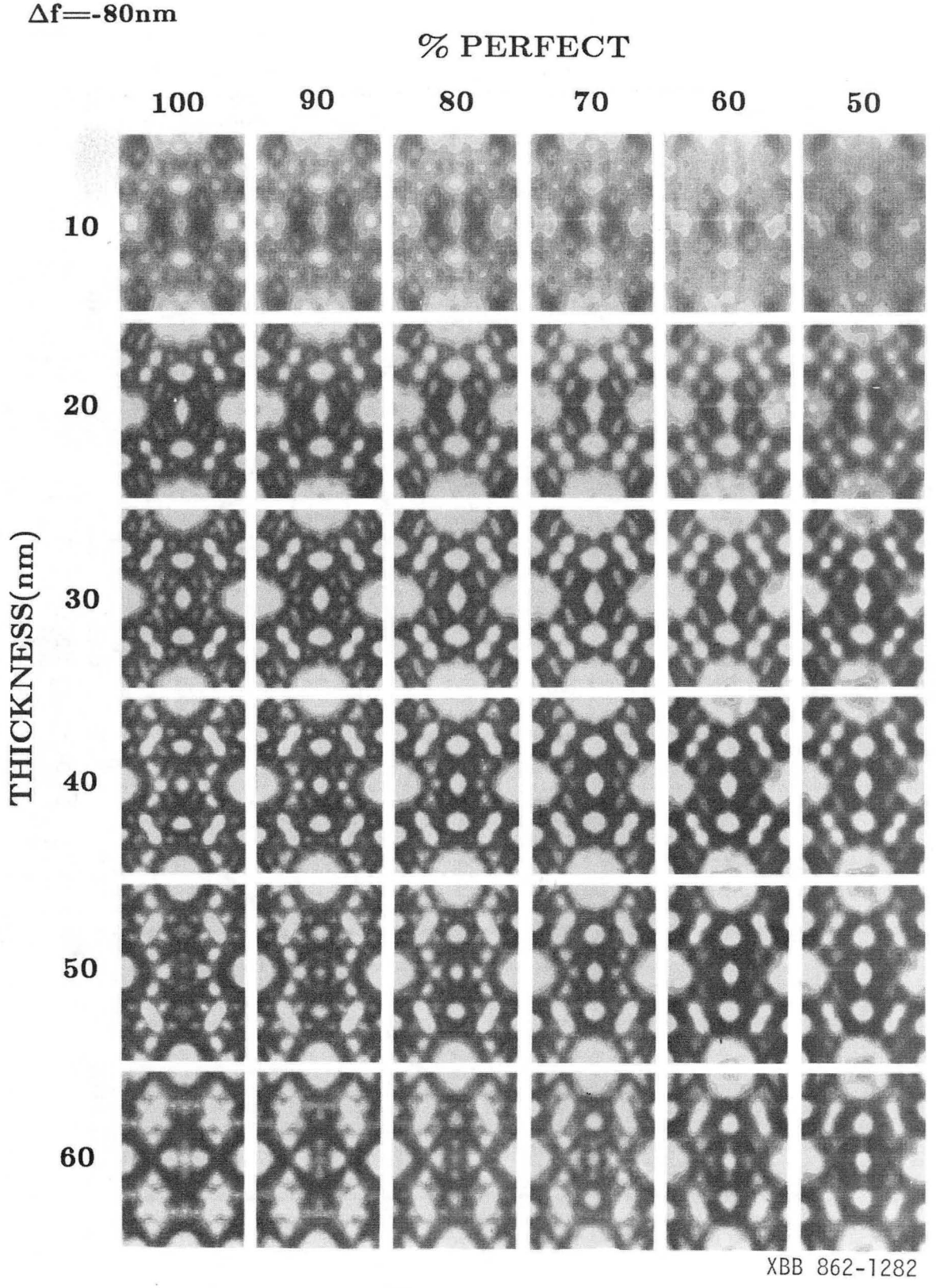
Δf=-80nm
% PERFECT
100
90
80
70
60
50
THICKNESS(nm)
10
20
30
40
50
60
XBB 862-1282

Fig. 15

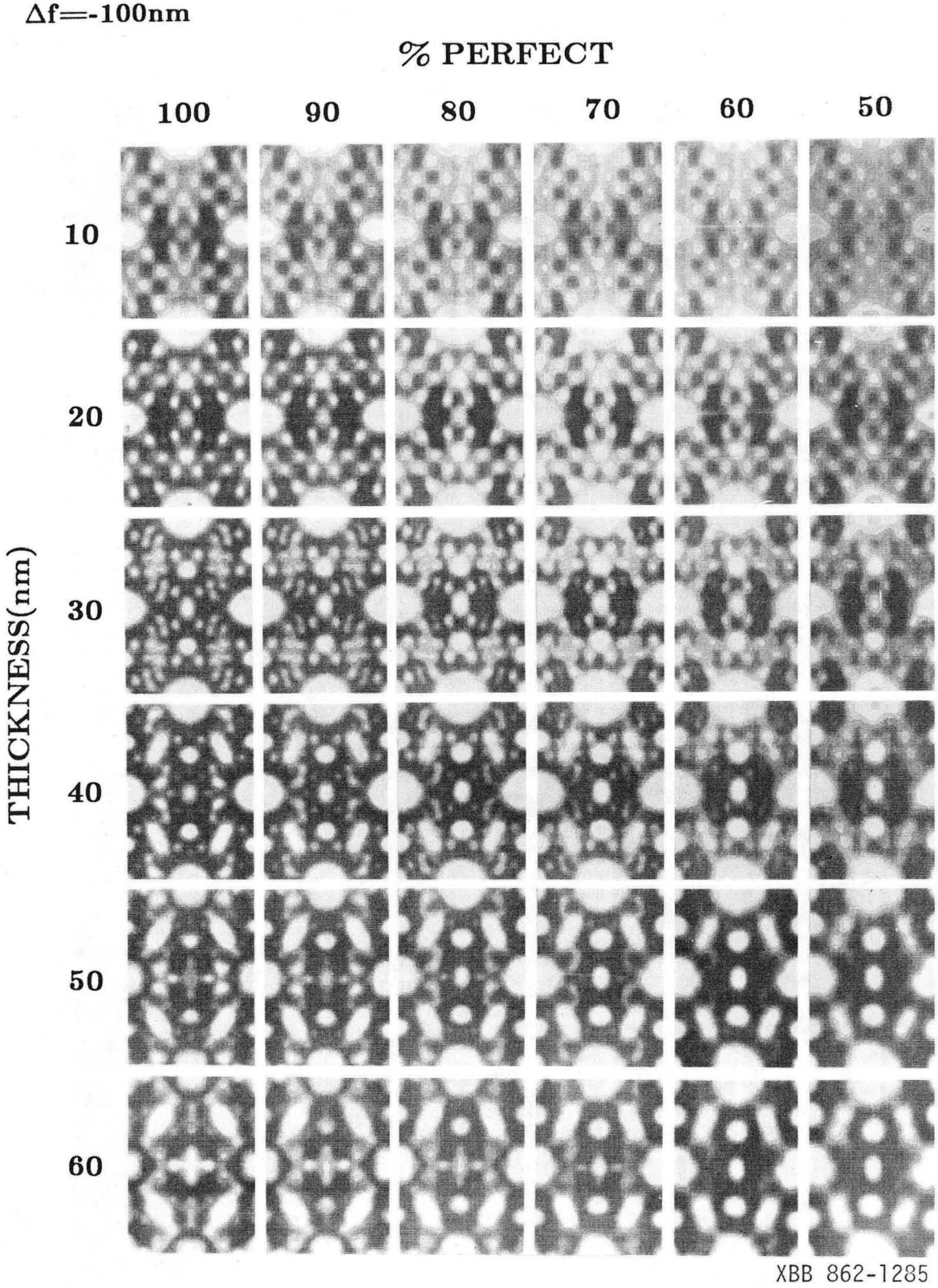
Δf=-100nm
% PERFECT
100
90
80
70
60
50
THICKNESS(nm)
10
20
30
40
50
60
XBB 862-1285

Fig. 16

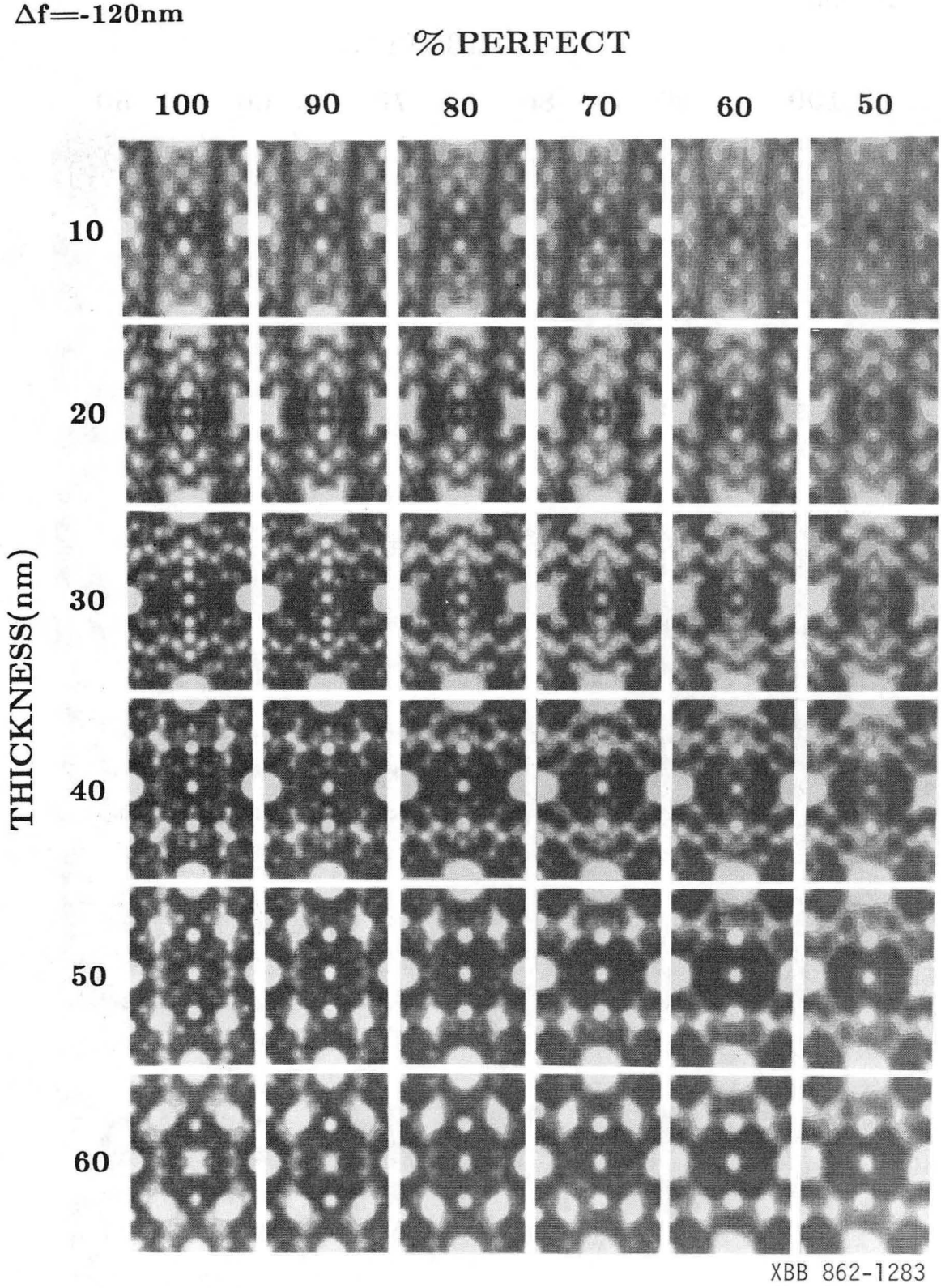
Δf=-120nm
% PERFECT
100
90
80
70
60
50
THICKNESS(nm)
10
20
30
40
50
60
XBB 862-1283

Fig. 17

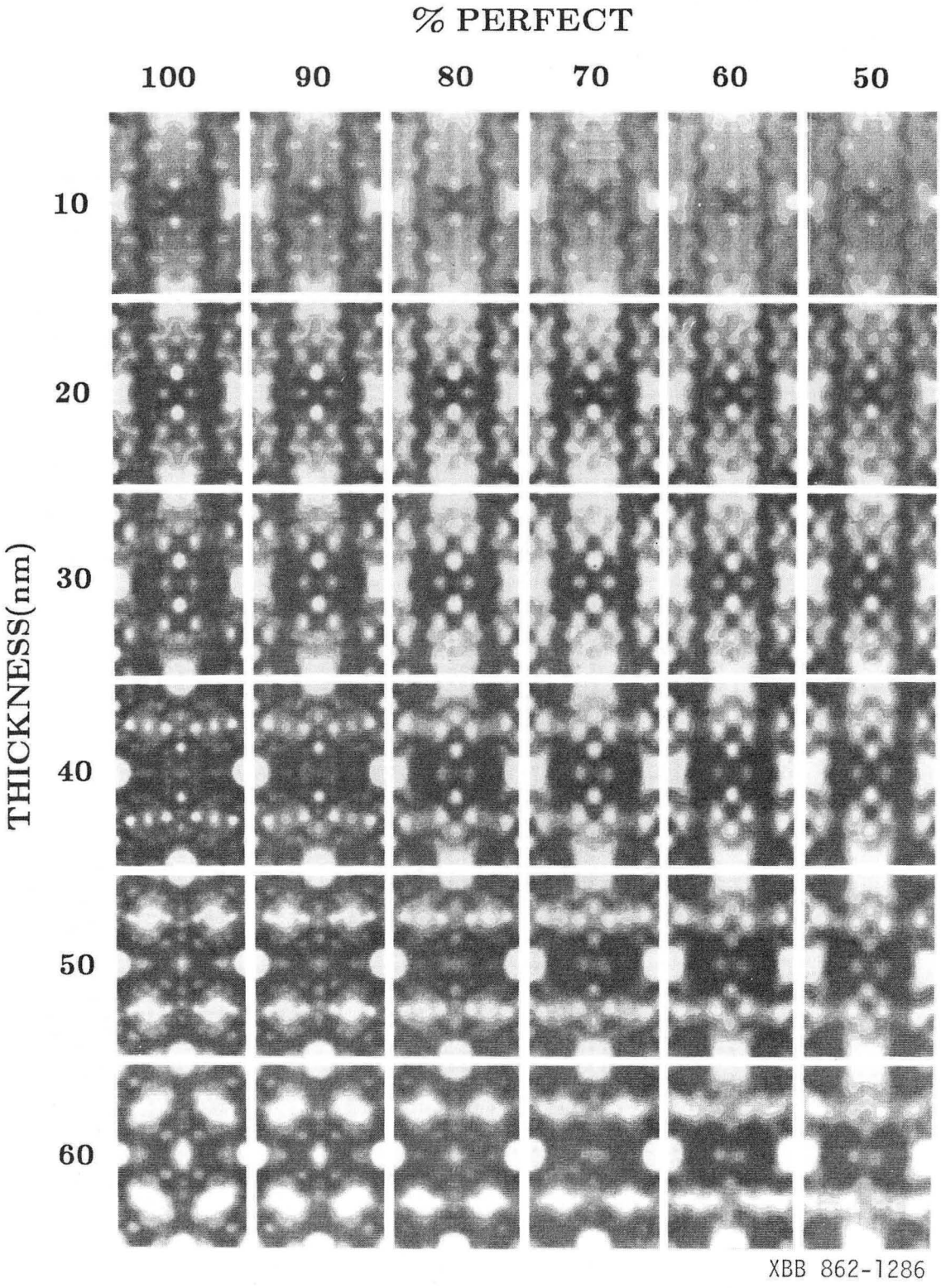
Δf=-140nm
% PERFECT
100
90
80
70
60
50
THICKNESS(nm)
10
20
30
40
50
60
XBB 862-1286

Fig. 18

*LAWRENCE BERKELEY LABORATORY*
*TECHNICAL INFORMATION DEPARTMENT*
*UNIVERSITY OF CALIFORNIA*
*BERKELEY, CALIFORNIA 94720*